APL Energy

REVIEW ARTICLE | JUNE 04 2025

Advanced Raman spectroscopy for battery applications: Materials characterization and *operando* measurements

Koji Hiraoka ; Yoshiki Yokoyama; Sarina Mine ; Kazuo Yamamoto ; Shiro Seki

APL Energy 3, 021502 (2025)
https://doi.org/10.1063/5.0272588

AIP Publishing

Advanced Raman spectroscopy for battery applications: Materials characterization and *operando* measurements

Cite as: APL Energy 3, 021502 (2025); doi: 10.1063/5.0272588
Submitted: 25 March 2025 • Accepted: 12 May 2025 •
Published Online: 4 June 2025

View Online Export Citation CrossMark

Koji Hiraoka,[1,2,a)] Yoshiki Yokoyama,[1] Sarina Mine,[3] Kazuo Yamamoto,[2] and Shiro Seki[1,a)]

AFFILIATIONS

[1] Graduate School of Applied Chemistry and Chemical Engineering, School of Advanced Engineering, Kogakuin University, 2665-1 Nakano-machi, Hachioji, Tokyo 192-0015, Japan
[2] Nanostructures Research Laboratory, Japan Fine Ceramics Center, 2-4-1, Mutsuno, Atsuta-ku, Nagoya 456-8587, Aichi, Japan
[3] JASCO Corporation, 2967-5, Ishikawa-machi, Hachioji, Tokyo 192-8537, Japan

[a)] **Authors to whom correspondence should be addressed:** koji-hiraoka@jfcc.or.jp and shiro-seki@cc.kogakuin.ac.jp.
Fax: +81-42-628-4568. **Tel.:** +81-42-628-4568

ABSTRACT

Raman spectroscopy is a powerful and versatile tool for battery research, elucidating the structural and bonding states of key components such as electrodes and electrolytes. This review highlights recent advancements in Raman spectroscopic techniques for both static material characterization and *operando* analysis of electrochemical reactions. Regarding static characterization, studies on the solvation structure of organic liquid electrolytes and the crystallographic analysis of electrode active materials are discussed. In addition, Raman-based image analysis is considered for visualizing the spatial distribution of structural components within composite electrodes. In Sec. III, we provide a comprehensive overview of ionic transport phenomena inferred from concentration variations, electrode degradation processes occurring during cycling, and the fundamental electrochemical reactions involved in electrode processes. Furthermore, a multi-scale analytical approach for all-solid-state sodium batteries has been introduced, enabling a comprehensive understanding of electrochemical processes from the atomic level to the μm scale. These advancements in Raman spectroscopy provide valuable insights into battery chemistry and significantly contribute to the development of next-generation energy storage systems.

NOMENCLATURE

ASSB	all-solid-state battery
AB	acetylene black
AF-ASSB	anode-free type all-solid-state battery
CV	cyclic voltammetry
CB	carbon black
DMC	dimethyl carbonate
EDS	energy dispersive x-ray spectroscopy
EC	ethylene carbonate
FT-IR	Fourier transform-infrared spectroscopy
G4	tetraethylene glycol dimethoxy ether
HCS	hard-carbon-bundled Si
HC	hard carbon
LIB	lithium-ion battery
LiFSA	$LiN(SO_2F)_2$
LiTFSA	$LiN(SO_2CF_3)_2$
LCO	$LiCoO_2$
LFP	$LiFePO_4$
Li-GIC	Li-graphite intercalated compound
MCR	multivariate curve resolution
NCO	$NaCoO_2$
NZSP	$Na_3Zr_2Si_2PO_{12}$
NNPP	$Na_4Ni_3(PO_4)_2P_2O_7$
NTP	$Na_3Ti_2(PO_4)_3$
NVP	$Na_3V_2(PO_4)_3$
PFG-NMR	pulse-field gradient nuclear magnetic resonance
R	height ratio of the G-band to the D-band

SPE	solid polymer electrolyte
SEM	scanning electron microscopy
SERS	surface-enhanced Raman spectroscopy
TOF-SIMS	time-of-flight secondary ion mass spectroscopy
TTE	1,1,2,2-tetrafluoroethyl 2,2,3,3-tetrafluoropropyl ether
TEM	transmission electron microscopy
XRD	x-ray diffraction
XAFS	x-ray adsorption fine structure

I. INTRODUCTION

In recent years, secondary batteries, including lithium-ion batteries (LIBs), have received significant attention in both academia and industry caused by the increasing global demand for renewable energy and a low-carbon society.[1–4] For battery development, various performance criteria are considered, such as high electric capacity, high operation voltage, high cycling capability, long lifecycle, and high thermal and electrochemical stability.[5–7] To address these requirements, numerous materials and cell configurations have been proposed[8–15] [e.g., electrode materials with high operating voltage/capacity, liquid/solid electrolytes with high ionic conductivity, and all-solid-state batteries (ASSBs)]. However, a fundamental and comprehensive understanding of these systems becomes increasingly challenging as material and cell structures become more complex, owing to both their physical complexity and the hierarchical reactions involved in the charge–discharge processes,[16–20] as illustrated in Fig. 1. Therefore, selecting the appropriate measurement method is essential to obtain reliable data and distinguish various physicochemical, electrochemical, morphological, and structural factors.

For the analysis of battery materials in their static state, structural evaluations of surfaces have been conducted using conventional techniques,[21–25] such as x-ray diffraction (XRD), Fourier transform infrared spectroscopy (FT-IR), and Raman spectroscopy. XRD and IR measurements are typically performed to clarify the crystal structures and intra/intermolecular interactions on material surfaces at the millimeter scale. Although Raman spectroscopy is also employed to examine molecular interactions and vibrational modes, it offers higher spatial resolution (on the order of micrometers), depending on the laser spot size. Higher resolution is

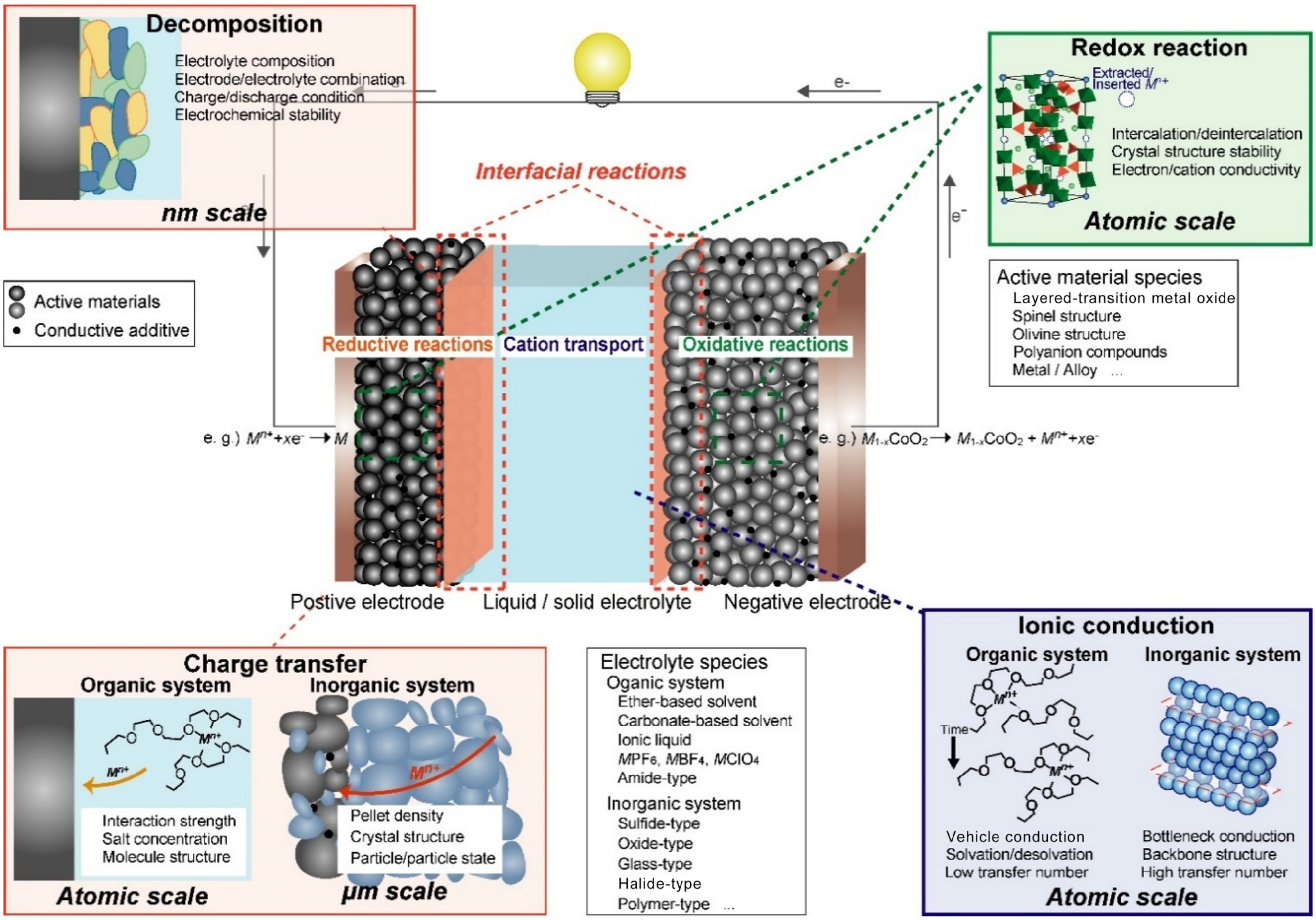

FIG. 1. Illustration of typical charge–discharge reactions occurring inside batteries.

advantageous for distinguishing structural information at the level of individual particles, probing electrode/electrolyte interfaces, and interrogating the interior/exterior of materials with more detail. In addition, Raman spectroscopy is effective for analyzing the carbon-based materials used in batteries, which are challenging to assess using IR methods owing to the principles of photon excitation processes.[26] Ultimately, Raman spectroscopy is versatile and can be applied to a wide range of materials, providing valuable structural information for the characterization of battery materials.

Recently, *in situ* and *operando* measurements have been gaining attention in the field of battery research because these techniques enable the observation of electrochemical reactions during operation.[27] *Operando* measurement techniques can elucidate various reaction steps occurring within component materials and the whole cell, clarifying the mechanisms and behaviors underlying inherent dynamic processes. As a result, the number of papers related to *operando* measurements in battery research has increased by more than ten times over the past decade. Our research group has been using *operando* Raman spectroscopy for reaction analysis in various battery systems because it provides relatively high spatial resolution, the ability to differentiate material components, and the capacity to observe structural changes at the atomic and molecular levels under dynamic conditions. In addition, quantitative analysis can be performed by applying curve fitting to the separated components of the Raman spectrum, as peak shapes are typically modeled using the *pseudo*-Voigt function, which combines Gaussian and Lorentzian profiles. In this review, we describe the approaches used to perform *operando* Raman spectroscopy in battery research, mainly focusing on case studies from our group, in addition to discussing the Raman-based evaluation of battery materials under static conditions.

II. RAMAN ANALYSIS FOR STATIC BATTERY MATERIALS CHARACTERIZATION

In the field of battery research, Raman spectroscopy is a common analytical technique for characterizing component materials, such as electrodes and electrolytes, to determine their molecular and atomic structures. This technique is comparable to IR spectroscopy and XRD, but Raman spectroscopy is mainly used to evaluate interactions and vibrational modes between intra and intermolecular structures, regardless of whether the material is crystalline or amorphous, organic or inorganic, and solid or liquid. This is a critical advantage in studying battery materials, which often include a diverse range of substances: polycrystalline active materials comprising carbon or metal oxides, conductive additives consisting of disordered or crystalline carbon, organic liquid and gel-like electrolytes, and solid electrolytes containing sulfides, oxides, or polymers. As the development of battery materials continues to advance rapidly, Raman spectroscopy becomes more important for analyzing a wide variety of compounds and clarifying local structures at the atomic level, including both particles and molecular structures. In this section, we focus on Raman measurements aimed at the general and advanced characterization of materials, including liquid electrolytes and electrode materials, under static conditions.

A. Raman spectroscopic insights into liquid electrolytes

Raman spectroscopy is useful for designing liquid-based electrolyte systems with beneficial viscosity, ionic conductivity, cationic transfer number, thermal stability, and electrochemical stability. Given that most liquid electrolytes are composed of alkali salts and organic solvents, their physiochemical and electrochemical properties are largely determined by their solvation structures and the electric interactions between intra and intermolecular components. Generally, the solvation structure is formed by the interaction between cations dissolved from the salt and solvent molecules, which contain ligands (e.g., oxygen and nitrogen atoms). Furthermore, solvated cations induce desolvation/solvation reactions at the electrode/electrolyte interfaces during charge–discharge cycles. Therefore, understanding solvation structures and their formation/interaction is essential for controlling the physicochemical and electrochemical properties of liquid electrolytes, considering that these factors directly impact electrode reactions and charge–discharge processes. Raman spectroscopy is advantageous for evaluating solvation structures and interactions because the vibrational states of solvent and anion molecules can be determined for various Raman-active bonds, such as C–O–C, C–C, and S–N–S. In particular, highly concentrated electrolyte systems garner significant interest owing to their high Li^+ transference number (t_{Li+}, over 0.5), which promotes rapid electrode reactions and extends the potential window to 5 V vs Li^+/Li.[28,29] Various studies have employed Raman to clarify the correlation between electrochemical properties and solvation structures. For example, Yamada *et al.* reported that a concentrated electrolyte consisting of $LiN(SO_2F)_2$ (LiFSA) as the salt and dimethyl carbonate (DMC) as the solvent can be applied to 5 V-class batteries.[30] This is attributed to the formation of a three-dimensional network comprising anions and solvent molecules, which exhibits strong coordination with Li^+, as evidenced by a combination of Raman spectroscopy and density functional theory-molecular dynamics simulations. In addition, Saito *et al.* combined Raman and synchrotron spectroscopy to detect the local structure in a complex liquid electrolyte system consisting of $LiN(SO_2CF_3)_2$ (LiTFSA) as the salt, tetraethylene glycol dimethoxy ether (G4) as the solvent, and 1,1,2,2-tetrafluoroethyl 2,2,3,3-tetrafluoropropyl ether (TTE) as a diluent.[31]

Furthermore, our research group has been investigating solvation structures and ionic transport mechanisms in superconcentrated liquid electrolytes using Raman spectroscopy and pulse-field gradient nuclear magnetic resonance (PFG-NMR).[32] The liquid electrolyte consisted of LiFSA as the Li salt and ethylene carbonate (EC) as the solvent, using various salt concentrations. Remarkably, the electrolyte maintained a liquid state with an EC-to-LiFSA molar ratio of 0.8:1.0 and exhibited a high t_{Li+} of ~0.63, as measured by PFG-NMR, despite its high viscosity [Fig. 2(a)]. To analyze the solvation structure of Li^+ in this highly concentrated electrolyte, we applied Raman spectroscopy across different salt concentrations, as shown in Fig. 2. The Raman spectra in the ranges of 880–930 cm^{-1} [Fig. 2(b)] and 660–810 cm^{-1} [Fig. 2(c)] correspond to the O–C–O stretching vibrations of EC and the S–N–S stretching vibrations of the FSA anion, respectively. Both vibrational modes depended on the salt concentration, indicating a predominance of solvated-EC and contact-ion pairs of the FSA anion with Li^+ for

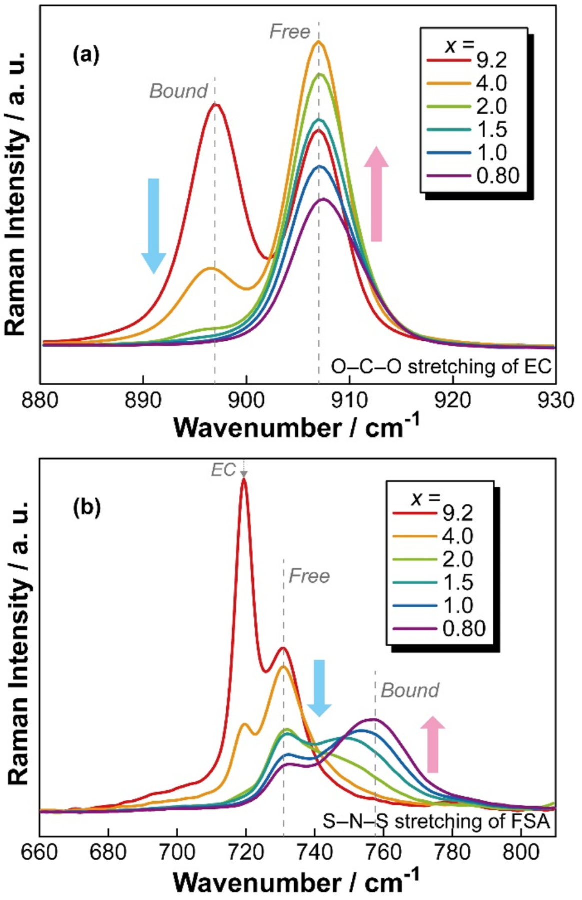

FIG. 2. Raman spectroscopy for a highly concentrated liquid electrolyte system under static conditions. (a) Raman spectra of *x*EC + LiFSA electrolytes in the 880–930 cm^{-1} range, corresponding to the O–C–O stretching vibration of EC. (b) Raman spectra of *x*EC + LiFSA electrolytes in the 660–810 cm^{-1} range, corresponding to the S–N–S stretching vibration of FSA. Reproduced with permission from R. Furui *et al.*, J. Phys. Chem. C **127**, 10748–10756 (2023). Copyright 2023 American Chemical Society.

[EC]/[Li] < 4. Furthermore, spin–lattice relaxation measurements performed using PFG-NMR revealed that the solvation structure involves not only EC but also the FSA anion, forming a bridge structure and facilitating a hopping-like Li$^+$ conduction mechanism, which contributes to the high $t_{\mathrm{Li}+}$ in highly concentrated regions.

These studies show that Raman spectroscopy is a powerful tool for evaluating the bonding and vibrational states of anions and solvents, thus revealing the solvation structure. These insights significantly contribute to the design of optimized liquid electrolyte systems, enhancing properties such as ionic conductivity and $t_{\mathrm{Li}}{}^+$.

B. Raman spectroscopic characterization of electrode materials

Electrodes generally consist of active materials, conductive additives, and binders, which contribute to redox reactions, electrical conductivity, and mechanical strength, respectively. In particular, the active material directly impacts battery performance by influencing capacity, operating voltage, and cycle capability. Thus, the development of advanced active materials is critical to achieving high performance in both liquid and solid-state battery systems.

Regarding negative electrode materials, graphite has a theoretical capacity of 372 mAh g^{-1} and is widely used because Li$^+$ can intercalate into the inner space between graphene layers.[33] To achieve higher capacities, silicon (Si)-based materials have been extensively studied in recent years, owing to their theoretical capacity of 4200 mAh g^{-1}, more than ten times that of graphite.[34] However, Si undergoes significant volumetric changes (~300%) during charging and discharge cycles, leading to severe capacity degradation due to continuous electrode decomposition and detachment from the current collector. To address this issue, our group proposed a hard-carbon-bundled Si (HCS) material consisting of multiple Si nanoparticles encapsulated by hard carbon (HC), which physically suppresses the volume change [Fig. 3(a)].[35] This design achieved a stable charge–discharge behavior with a coulombic efficiency of 99% for over 100 cycles, without significant electrode exfoliation. However, determining the structure of HCS is relatively challenging because it consists of amorphous carbon and Si nanoparticles. Therefore, we applied Raman spectroscopy to detect both the HC and Si phases. As shown in Fig. 3(b), the Raman spectra of HC and HCS powders (where HC-2 and HCS-2 represent samples carbonized at higher temperatures than HC-1 and HCS-1) revealed a distinct peak at 520 cm^{-1} and broad bands at 1350 and 1600 cm^{-1}, corresponding to Si and HC. These results demonstrate that Raman spectroscopy can be used to simultaneously evaluate both the Si and HC phases, even when using nanoparticles and amorphous carbon. This is particularly beneficial considering the challenges associated with XRD, resulting in a broad, indistinguishable peak (i.e., a halo peak), which hinders characterization. Hence, Raman spectroscopy can capture structural and bonding information from powders containing multiple material species, such as Si nanoparticles and amorphous HC.

In positive electrodes in LIBs, the active materials commonly contain layered transition metal oxides, such as $LiCoO_2$ (LCO) and $LiNi_xMn_yCo_zO_2$ ($x + y + z = 1$). These materials exhibit a stable charge–discharge behavior, with capacities of 137 and 140–160 mAh g^{-1}, respectively, at an operating voltage of 4 V. These materials allow for the reversible intercalation of Li$^+$ into the internal spaces between MO_2 layers (M: transition metal) during charge–discharge cycles. Therefore, the crystal structure of these active materials plays a critical role in determining the reversibility and electrochemical stability of the charge–discharge reactions. Although ordered structures are typically evaluated by XRD, there are several limitations concerning composite electrode sheets. In particular, the wide irradiation area of x rays (on the millimeter scale) often includes contributions from the current collector, making it challenging to analyze thin and highly porous electrodes.

We applied Raman spectroscopy to study composite electrode sheets in Na-based ASSBs using solid polymer electrolytes (SPEs).[36] Na-based batteries are being developed as next-generation batteries owing to the natural abundance of Na, which has a Clarke number that is over 500 times higher than that of Li, offering a promising alternative to LIBs. In our Na-based ASSBs, the positive electrode consisted of $NaCoO_2$ (NCO), an active material with a crystal structure similar to that of LCO (O3-type); acetylene black (AB), a conductive additive; and poly(ethylene oxide/methoxyethoxy ethyl

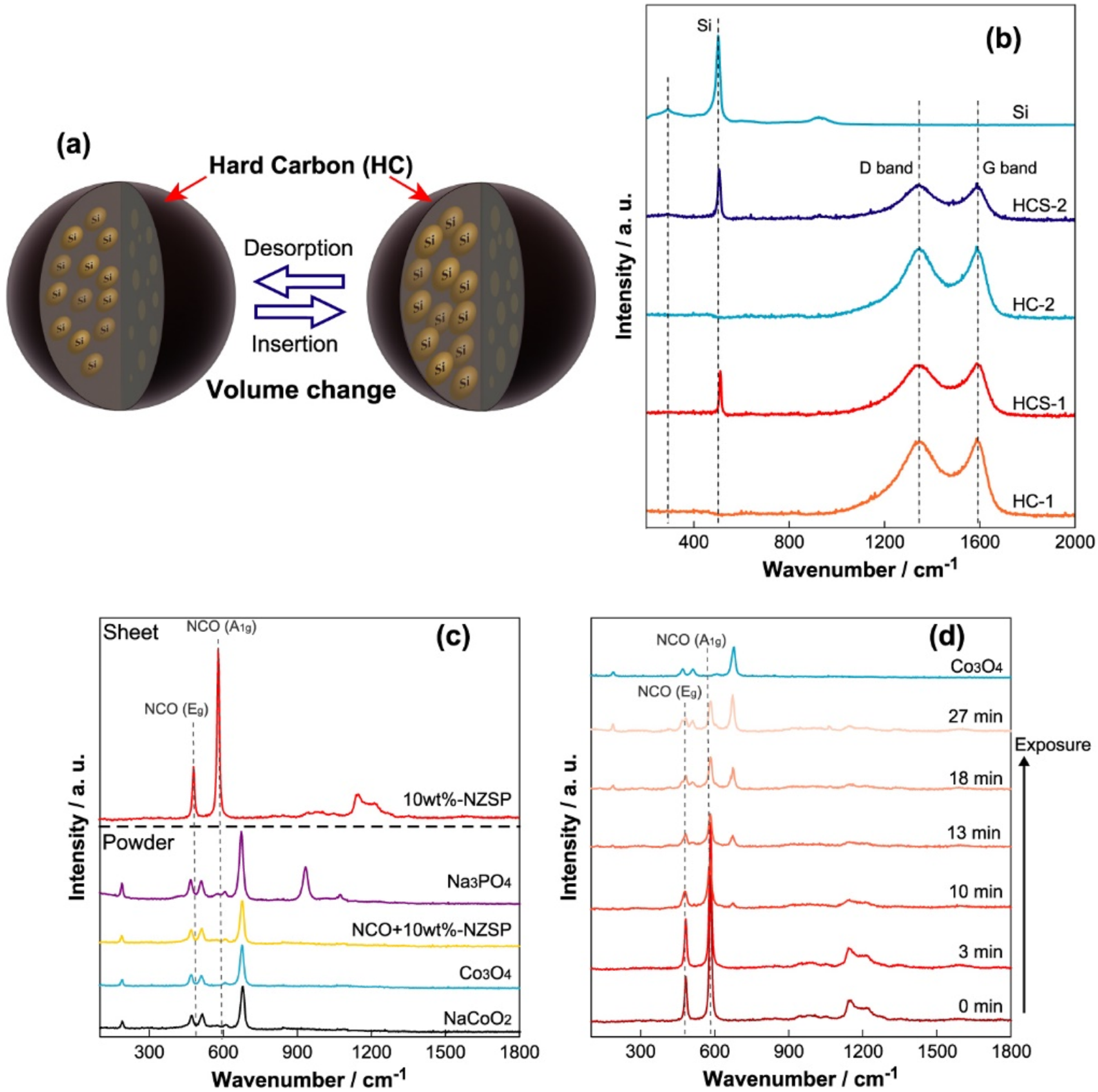

FIG. 3. Raman spectroscopy for two types of electrode active materials (HCS and NCO) under static conditions. (a) Illustration of the HCS active material consisting of multiple Si nanoparticles and amorphous HC phases. (b) Raman spectra of HC and HCS in the 200–2000 cm^{-1} range, in which HC-1 and HCS-1 have lower carbonization temperatures than those of HC-2 and HCS-2. Reproduced with permission from U. Tsunoda *et al.*, Mater. Adv. **4**, 4436–4443 (2023). Copyright 2023 Royal Society of Chemistry. (c) Raman spectra of the 10 wt. % NZSP-coated NCO electrode sheet and the reference materials (upper), and time dependence of the spectra for the non-coated NCO electrode sheet with air exposure (lower). Reproduced with permission from T. Ichikawa *et al.*, RSC Adv. **14**, 19726–19734 (2024). Copyright 2024 Royal Society of Chemistry.

glycidyl ether)-NaTFSA, a binder. NCO operates at a relatively high voltage of ~3.7 V vs Na$^+$/Na and exhibits a theoretical capacity of 117 mAh g^{-1}. However, NCO is highly susceptible to decomposition and crystal structural collapse upon exposure to moisture, forming Co_3O_4 as a side product. As shown in the top part of Fig. 3(c), Raman spectra of powder samples [pure NCO, pure Co_3O_4, and 10 wt. %-$Na_3Zr_2Si_2PO_{12}$ (NZSP)/-Na_3PO_4-coated NCO] revealed peaks for Co_3O_4 at 194, 488, 522, and 691 cm^{-1},[37] even though storage and measurements were performed under Ar atmosphere. In contrast, the composite electrode sheet using 10 wt. %-NZSP-coated NCO showed distinct peaks at 490 and 590 cm^{-1}, corresponding to the E_g (twist vibration of O–Co–O) and A_{1g} (symmetric stretching vibration of Co–O) modes in layered oxides.[38] Notably, these Raman spectra did not include peaks or fluorescence from the Al current collector, indicating that the measurement only involved the electrode surface. These results suggest that Co_3O_4 formation was eliminated during the preparation of the composite electrode, including powder mixing and the addition of an organic solvent as a dispersant. To further analyze this, Raman spectroscopy was performed on non-coated NCO composite electrode sheets exposed to air for different durations, as shown in the bottom part of Fig. 3(c). Initially, the Raman spectra showed the NCO-related peaks at 490 and 590 cm^{-1}, but these peaks disappeared after 10 min, replaced by new peaks attributed to Co_3O_4. This demonstrates that NCO exhibits low chemical stability, as revealed by changes in the crystal structure and bonding states via Raman spectroscopy.

In summary, Raman spectroscopy reveals valuable structural information for bulk battery materials, including liquid electrolytes, active material powders, and composite electrode sheets, under static conditions. It is particularly useful for elucidating the solvation structure of liquid electrolytes, the crystal structure of the active materials, and chemical stability as a function of air exposure time.

C. Raman-based image analysis

Secondary batteries, including LIBs, contain current collectors that support the positive and negative electrode materials, and these electrodes are separated by a porous material impregnated with an electrolyte. Each electrode is composed of several materials, including active materials that store and release Li$^+$, conductive additives that aid electron transfer between active materials, and binders that hold the components together. The properties of the electrodes, which depend on the mixing ratios and dispersion states of these materials, significantly influence battery performance. Consequently, evaluating the battery performance requires not only electrochemical characterization via charge–discharge tests but also a comprehensive assessment of the electrode properties, including the dispersion states and crystal structures of each component. Electron microscopy techniques, such as scanning electron microscopy (SEM) and transmission electron microscopy (TEM), combined with energy dispersive x-ray spectroscopy (EDS) for elemental analysis, are commonly used for these purposes.[24]

We combined two-dimensional (2D) imaging of the electrode sheets with Raman spectroscopy to determine the distribution of electrode materials. The measurement results were analyzed using multivariate curve resolution (MCR), thereby extracting component-specific information from composite electrodes and calculating the principal component spectra. This approach helped visualize the aggregation and dispersion states of each component in the composite electrode with a spatial resolution of less than 1 μm.

Figure 4(a) shows the individual Raman spectra of the principal components in the positive electrode: LCO, $LiFePO_4$ (LFP), and AB. Because LFP was coated with carbon, bands corresponding to the G- and D-bands of carbon were observed at 1600 and 1350 cm^{-1}, respectively, similar to those found in the carbonaceous material AB. In addition, a band corresponding to the symmetrical stretching mode of PO_4^{3-} in LFP appeared near 954 cm^{-1}.[39] Figures 4(b) and 4(c) show an optical microscopy image of the electrode sheet and a color-coded map generated from the spectral intensity of each component distinguished by MCR. Using this approach, we revealed the distribution of AB and LFP based on structural and vibrational information in the composite electrode sheet.

III. *OPERANDO* RAMAN SPECTROSCOPY

In all battery systems, there are correlations between the electrochemical reactions involved in electrode redox processes, or the

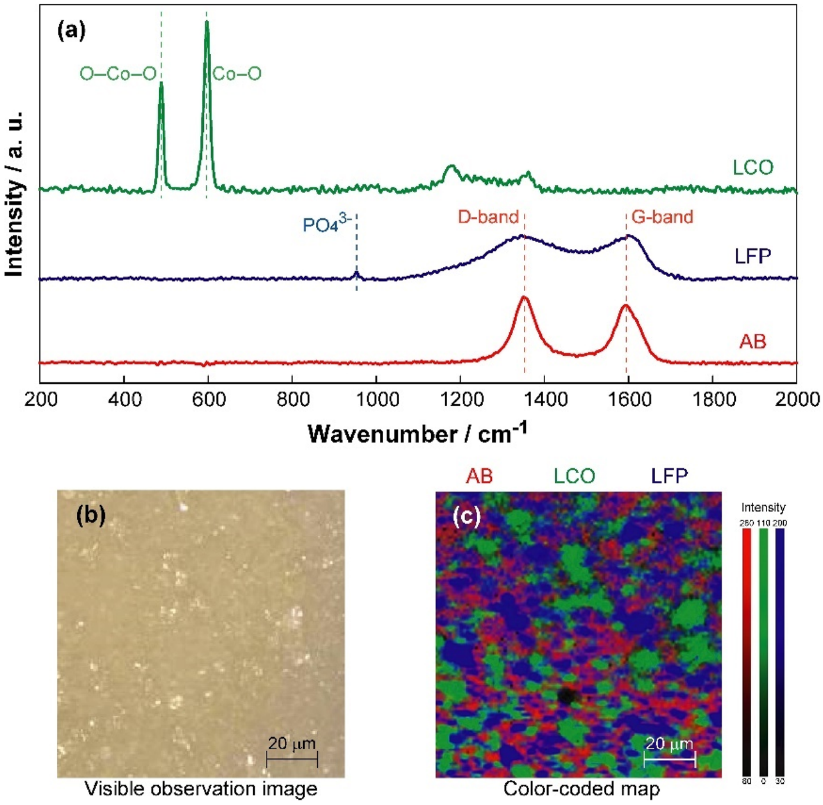

Visible observation image

Color-coded map

FIG. 4. Image analysis for evaluating the distribution of component materials in the composite electrode sheet, consisting of the LCO, LFP, and AB. (a) Individual Raman spectra of the principal components. (b) Optical microscopy image of the electrode sheet. (c) A color-coded map generated from the spectral intensity of each component distinguished using the MCR method.

ionic transport within the electrolyte, and the structural, morphological, and physicochemical changes of the component materials and/or their interfaces. These correlations are critical and represent significant hierarchical steps in battery operation. Before the 2010s, these relationships were primarily evaluated indirectly using *ex situ* measurement techniques, which rely on cell assembly/disassembly, material extraction, and similar processes to interrogate different stages in the battery lifecycle.[21,27,40] However, *ex situ* measurements involve risks related to the sample transfer, alterations under electrochemical conditions, and structural changes caused by external impacts and applied stress. In contrast, *operando* (or *in situ*) measurement techniques enable direct observation of structural and morphological changes, as well as alterations in physicochemical properties, while the electrochemical reactions occur during standard operation. These measurements are achieved through careful sample preparation and cell design for specific spectroscopic and analytical methods. Accordingly, the visualization of battery reactions using *operando* measurements has been intensively studied in recent years.[21,41–43]

Several *operando* analysis techniques have been widely applied, including XRD, x-ray adsorption fine structure (XAFS), x-ray computed tomography (CT), SEM, TEM, IR, and Raman spectroscopy.[44–53] These techniques are chosen based on the specific objectives of the measurement and are valued for their adaptability and high resolution (time, spatial, or spectral), supporting the analysis of numerous battery systems. Raman spectroscopy, in particular, can be performed under atmosphere environmental conditions and distinguish between electrode and electrolyte layers, as well as acquire data along the thickness direction, with a relatively high spatial resolution of ~1 μm. This capability allows for the detailed examination of various phenomena, such as crystal structure changes associated with redox reactions, concentration changes linked to ionic transport, and interphase formation during the charge transfer process inside the electrode, electrolyte, and their interfaces. In addition, surface-enhanced Raman spectroscopy (SERS) is increasingly being utilized to analyze battery materials and the decomposition phases formed at the electrode/electrolyte interface. The SERS method enhances the Raman signal by employing Ag or Au substrates and their nanoparticles dispersed in solution.[54] For example, the formation process of decomposition phases was observed using SERS and SiO_2-coated Au nanoparticles under charge–discharge operation in a [Li|liquid electrolyte|SiO_2] cell, as reported by Hy *et al.*[55]

Herein, we introduce recent progress in *operando* Raman spectroscopy research, focusing on the evaluation of electrochemical and charge–discharge reactions in various ASSB systems. This section primarily summarizes *operando* Raman spectroscopy studies in solid-state battery systems. In liquid-based cells, leakage and convection of the liquid electrolyte present technical challenges and may hinder fundamental understanding of electrochemical reactions.

A. Analysis of ionic transport in polymer electrolytes

During charge–discharge operations, in both liquid and solid systems, the ionic transport process inside the electrolyte plays a critical role in enabling electrode reactions such as the insertion/extraction and deposition/dissolution of carrier ions (e.g., Li^+ and Na^+). In conventional electrolyte systems (excluding inorganic solid electrolytes), the electrolyte consists of cations and anions derived from dissolved metal salts, along with a solvent (ligand molecules). As the carrier ions are charged, cations and anions migrate between the positive and negative electrodes (working and counter electrodes) during electrochemical or charge–discharge reactions, driven by an applied potential or electric current. At the electrode/electrolyte interface, only the carrier ions (typically cations) participate in redox reactions, leading to localized concentration gradients (diffusion layers) and concentration polarization. This occurs because counterions (anions) are not involved in redox reactions. Such localized concentration changes become significant in electrolytes with low t_+, resulting in reduced charge–discharge rates and lower battery performance due to the slow ionic transport of the carrier species. The t_+ is typically evaluated using electrochemical methods (e.g., DC polarization and low-frequency impedance) and PFG-NMR. However, the dynamic ionic conduction mechanism, particularly under operating conditions, has not been fully clarified. In recent years, several research groups have leveraged *operando* Raman spectroscopy techniques to elucidate ionic transport mechanisms in organic-based electrochemical cells. For liquid electrolyte systems, Fawdon *et al.* applied *operando* Raman spectroscopy to evaluate concentration changes during constant current operation and relaxation in a [metallic Li|LiFSA/G4|metallic Li] symmetrical cell using an inverted glass tube-type cell design with a verticality aligned laser/objective lens.[56] They demonstrated that the observed changes in the integrated peak intensity of the S–N–S vibrational mode (from the anion) near the electrodes correlated well with theoretical diffusion models. Ishino *et al.* used *operando* Raman spectroscopy to study changes in the solvation structure at the interface of a $NaCrO_2$-based positive electrode/Na-conductive ionic liquid (IL) electrolyte under various salt concentrations.[57] They found that a highly concentrated IL electrolyte maintained its initial solvation structure during discharge, which suppressed Na^+ depletion at the electrode/electrolyte interface. In gel and solid polymer electrolyte systems, Rey *et al.* evaluated salt concentration changes in Li-based symmetrical cells using polyethylene oxide as the polymer host and LiTFSA as the Li salt,[58] revealing that the salt concentration increased near the counter electrode and decreased near the working electrode under constant current, strongly correlating with current density. Similarly, Georén *et al.* performed *operando* Raman spectroscopy on polyether-based electrolytes in Li-based symmetrical cells, confirming that concentration changes aligned with theoretical calculations.[59] Despite the ability to observe ionic transport phenomena using *operando* Raman spectroscopy, differences in the concentration change behavior among cationic species under dynamic conditions during electrochemical reactions remain unclear.

To address this, we investigated the ionic transport mechanism in SPE systems, focusing on the differences between Li- and Na-based systems.[60] SPEs consist of a host polymer network and dissolved metal salts, enabling ionic transport by cationic migration according to segmental motion in the solvated complexes. By selecting different metal salts, SPEs can be designed as cation-conductive electrolytes for Li^+ or Na^+. In our previous study, we prepared Li- and Na-conductive SPEs using a polyether-based macromonomer with LiTFSA or NaTFSA as the metal salt. Ionic transport behavior was evaluated under constant voltage application in [metallic Li or Na|SPE|metallic Li or Na] symmetrical cells. The measurement cell for *operando* Raman spectroscopy contains a quartz glass observation window, stainless-steel electrodes with adjustable pressure using a spring, and three external electrodes, as shown in Fig. 5(a). Symmetrical cells were prepared by stacking a metallic electrode on a Cu current collector (9 × 9 mm^2) with an SPE film (~500 μm thick) and inserting the assembly into the measurement cell [see Fig. 5(a)]. In this configuration, cations were deposited on the counter electrode side and dissolved on the working electrode side. Figure 5(b) shows the typical Raman spectra of Li- and Na-based SPEs, corresponding to the SNS-CF$_3$ vibrational mode in the TFSA anion under static conditions. Considering that the integrated intensities correlate with salt concentration ([M]/[O]), these peaks were used to

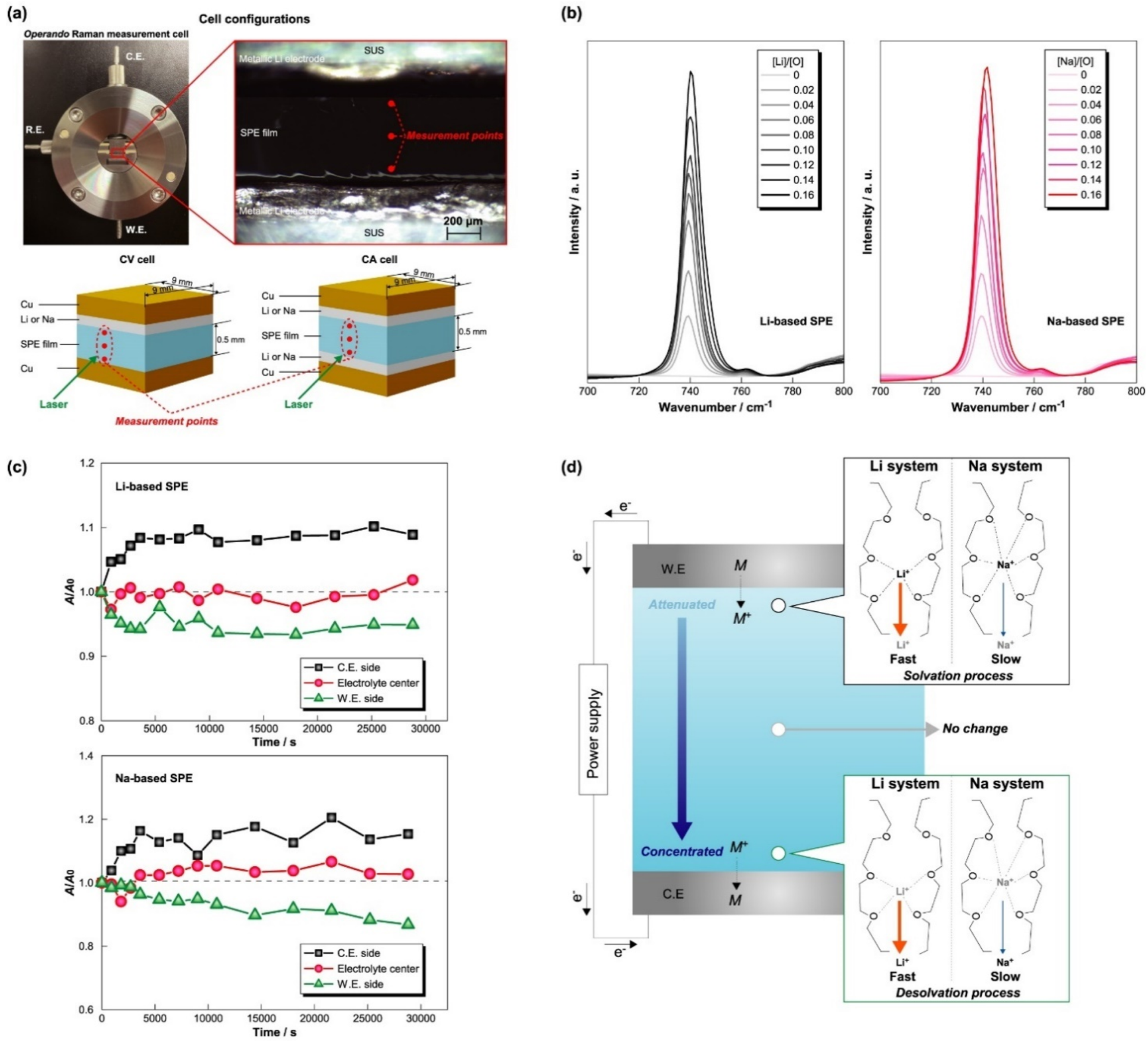

FIG. 5. Using *operando* Raman spectroscopy of Li/Na symmetrical cells to clarify the ionic transport mechanism with concentration changes inside the SPE. (a) Image of the *operando* Raman cell with the quartz glass observation window and the cross-sectional image with illustrations of the cell structure and CV measurement points. (b) Typical Raman spectra of the Li- and Na-based SPEs in the 700–800 cm^{-1} range, corresponding to the SNS-CF$_3$ vibration of the TFSA anion. (c) Relationship between the applied voltage time and A/A_0, normalized by the integrated intensity of the initial state for the TFSA peak, corresponding to the changes in salt concentration near the electrodes. (d) Illustration of the concentration changes based on ionic transport induced by solvation/desolvation processes in the Li- and Na-based SPEs during electrochemical reactions. Reproduced with permission from K. Hiraoka *et al.*, J. Phys. Chem. C **127**, 11864–11874 (2023). Copyright 2023 American Chemical Society.

determine the concentration changes during electrochemical reactions. Under an applied voltage, Raman spectra were collected near the working electrode, counter electrode, and center of the electrolyte. The integrated intensities were calculated by curve fitting and normalized to their initial values (A/A_0) for quantitative evaluation. In Li-based cells, A/A_0 increased near the working electrode, decreased near the counter electrode within 1 h, and then maintained constant values, as shown in Fig. 5(c). This indicates that significant concentration changes occurred because of Li^+ deposition and dissolution, reaching a steady state under constant voltage. In contrast, Na-based cells exhibited slight, continuous changes at both electrodes [see Fig. 5(c)]. This behavior is likely due to the larger ionic radius of Na^+ compared with that of Li^+, which leads to a more stable solvation structure with ether oxygen and slower ionic transport during electrochemical reactions. The differences in solvation structure also contribute to the observed concentration changes during ionic transport under dynamic conditions in Li- and Na-based SPEs, as illustrated in Fig. 5(d). In summary, *operando* Raman spectroscopy can reveal the changes in the salt concentration and, thus, help explain the ionic transport mechanisms, by associating peak shifts with the behavior of anions and ligand molecules.

B. Degradation analysis in oxide-based all-solid-state batteries

Degradation analysis is critical for promoting the development of practical battery systems. Almost all types of batteries, including liquid- and solid-based systems, exhibit degradation in electrical capacity, operating voltage, and resistive properties owing to the operation duration, voltage range, high temperatures, and atmospheric exposure. Moreover, battery degradation generally occurs in all components (e.g., electrodes, electrolytes, and interfaces) and involves multiple materials (e.g., active materials, conductive additives, electrolyte additives, and organic solvent molecules). Many researchers have studied degradation processes and mechanisms using various electrochemical measurements, such as charge–discharge tests, cyclic voltammetry (CV), AC impedance, and storage tests,[61] but these methods have limitations in terms of quantitative detection and observing local degradation. Consequently, *operando* measurement techniques are valuable for directly evaluating degradation phenomena by visualizing morphological, structural, and elemental changes during electrochemical reactions. In particular, Raman spectroscopy offers spatial resolution at the micrometer scale, which is determined by the excitation laser spot size, allowing for separate observations of the electrode and electrolyte layers. Furthermore, when the spectroscopic features of each material are assigned, changes in bonding states and crystal structures within the composite electrode layer can be analyzed. Utilizing these advantages, *operando* Raman spectroscopy has been applied to target dynamic changes in the structural and bonding states of electrode active materials. Flores *et al.* reviewed *operando* Raman spectroscopy for various active materials, including layered transition metal oxides ($LiMO_2$: M = Co, Ni, Mn).[52] However, reports on capacity degradation remain limited. Li *et al.* analyzed the degradation of graphite (C_6)-based electrodes in a [C_6|liquid electrolyte|$LiFePO_4$] cell by performing *ex situ* Raman spectroscopy in the pristine and cycled (over 200 cycles) states.[62] In contrast, we conducted *operando* Raman spectroscopy for degradation analysis in ASSBs during charge–discharge operations, building on our previous work.[63]

In particular, *operando* Raman spectroscopy was applied to an ASSB consisting of $Na_4Ni_3(PO_4)_2P_2O_7$ (NNPP) and $Na_3Ti_2(PO_4)_3$ (NTP) as active materials for the positive and negative electrodes, respectively, and NZSP as the solid electrolyte. NNPP contains PO_4 tetrahedra, NiO_6 octahedra, and $P_2O_7{}^{4-}$ pyrophosphate anions, offering a high operating voltage exceeding 4 V vs Na/Na^+, derived from the Ni^{3+}/Ni^{2+} redox couple.[64] NTP has a superionic conductor structure, containing PO_4 tetrahedra and TiO_6 octahedra that share corner oxygens, and features two redox couples, Ti^{3+}/Ti^{4+} and Ti^{3+}/Ti^{2+}.[65] Both NNPP and NTP are promising for high-performance Na-based ASSBs, but their charge–discharge mechanisms and degradation behavior during cycling remained unclear. To address this, we applied *operando* Raman spectroscopy to the cross section of an ASSB during the first few charge–discharge cycles. The ASSB was physically split and polished under an Ar atmosphere using cross section polisher equipment with Ar^+ milling. This milling process played a key role in enabling *operando* measurements because a flat surface was required to obtain clear spectra and reliable data without interference from sample roughness [Fig. 6(a)]. The Raman spectra of the powder and sintered samples are shown in Fig. 6(b). The Raman spectra of NZSP in the solid electrolyte form remained similar to those in the powder form, whereas the spectra of the positive and negative electrode layers containing NNPP and NTP exhibited significant broadening, suggesting that structural changes were induced by spark plasma sintering. The charge–discharge CV profile is presented in Fig. 6(c), showing current peaks at 3.0 and 3.5 V during charging and 3.0 V during discharging. These current peaks indicate significant irreversible capacity during the first cycle and degradation with cycling, as evidenced by broader and decreasing current values, especially for the first cycle. However, it was difficult to understand the degradation mechanism based on only the CV profile, and Raman spectra were acquired from the center of the positive electrode, negative electrode, and solid electrolyte layers in the ASSB cross section during charge–discharge cycles, as shown in Fig. 6(d). The solid electrolyte maintained a pristine state over the three charge–discharge cycles, indicating a stable crystal structure in the central region during Na^+ transport between electrodes. In contrast, the Raman spectra of the positive and negative electrode layers showed irreversible changes from their pristine states during the first charge–discharge cycle. These results imply that the crystal structures of NNPP and NTP transition to metastable states, contributing to decreased electrochemical activity and capacity. Furthermore, the Raman spectra during the third cycle did not change, suggesting the formation of unreactive crystal structures in NNPP and NTP. These irreversible crystal structures directly influence capacity degradation during cycling. Overall, *operando* Raman spectroscopy is effective for evaluating degradation mechanisms in ASSBs by observing crystal structure changes at the sub-micrometer scale.

C. Carbon structural changes in sulfide-based all-solid-state batteries

In next-generation secondary batteries, carbon materials play important roles as conductive additives with disordered structures [e.g., AB, ketjen black, carbon black (CB), and carbon nanotubes] in

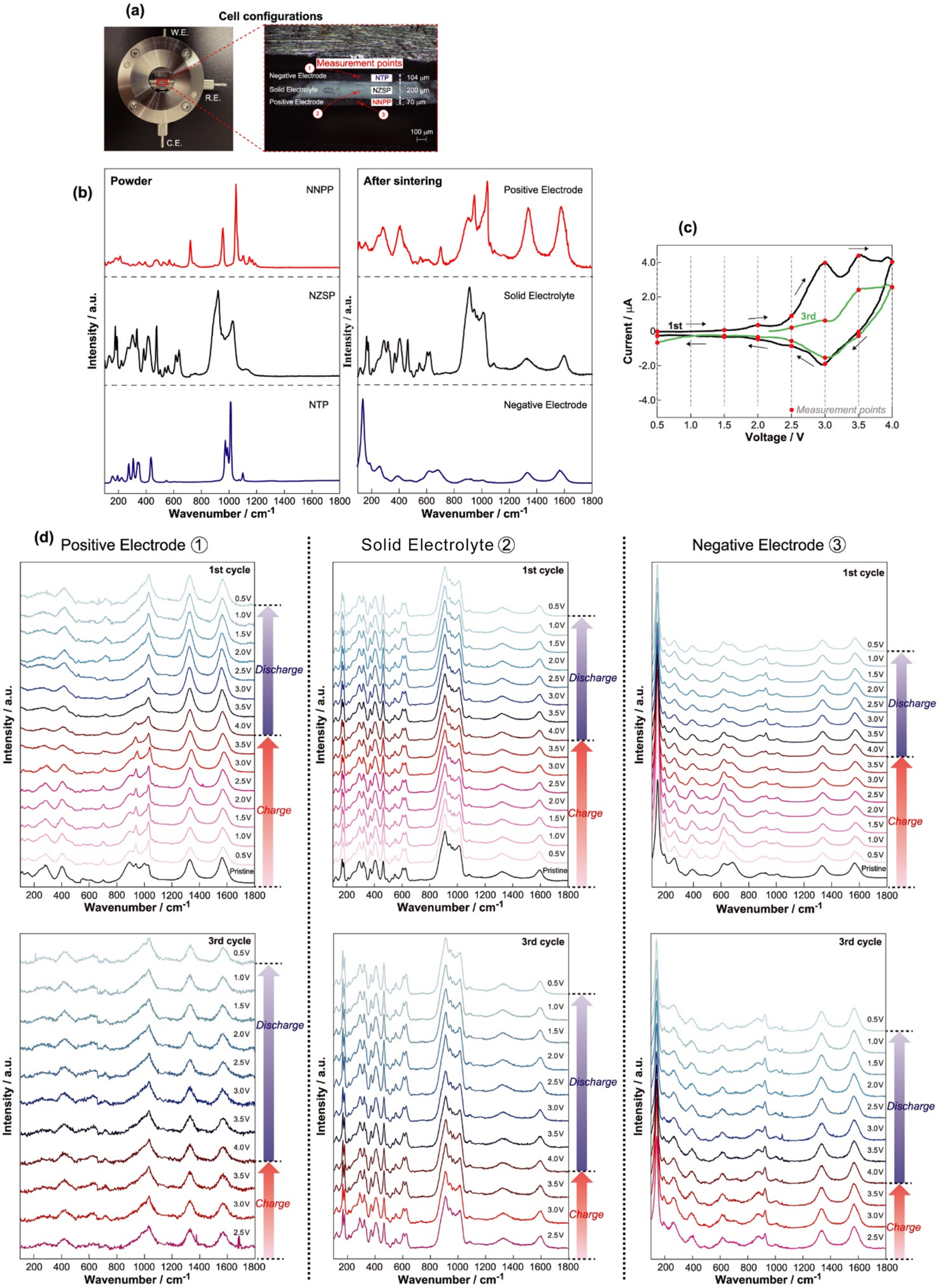

FIG. 6. Using *operando* Raman spectroscopy of an oxide-type Na-ASSB with NNPP and NTP as the positive and negative electrode active materials, respectively, to evaluate the degradation process with cycling. (a) Configuration of the *operando* Raman cell and the cross-sectional image with the measurement points located in the center of the positive electrode, solid electrolyte, and v layers. (b) Raman spectra of the NNPP and NTP powders, as well as the positive and negative electrode layers in the cross section after sintering. (c) *Operando* Raman spectroscopy and CV with a scan rate of 0.3 mV s^{-1} and voltage range of 0.5–4.0 V during three charge–discharge cycles, showing the current decrease with cycling. (d) *Operando* Raman spectra taken every 0.5 V for the positive electrode, solid electrolyte, and negative electrode layers during the first and third charge–discharge cycles. Reproduced with permission from T. Ono *et al.*, ACS Appl. Energy Mater. **6**, 6194–6200 (2023). Copyright 2023 American Chemical Society.

composite electrodes and as active materials with high crystallinity (e.g., graphite and HC), enabling intercalation and deintercalation of carrier ions. Graphite with high crystallinity is mostly used as the active material in negative electrodes for various battery systems, including commercial LIBs, because of its reversible reactions during Li^+ intercalation and deintercalation, involving the formation of Li–graphite intercalated compounds (Li–GICs). Graphite is composed of sp^2 hybrid orbitals and is well known for its strong Raman band near 1580 cm^{-1}, attributed to the E_{2g} mode at the Brillouin zone center, commonly referred to as the G-band.[26,66] In 1995, Inaba *et al.* demonstrated that the G-band shifts to lower wavenumbers and splits into two components during Li^+ intercalation in graphite, as observed by *in situ* Raman spectroscopy in a liquid electrolyte-based half-cell.[67] This phenomenon supported earlier findings from *in situ* XRD measurements and the stage model, which describes the formation of multiple graphite structures during Li^+ intercalation.[68] Since then, *operando* Raman spectroscopy has frequently been used to evaluate structural changes in graphite-based materials.

In recent years, amorphous and disordered carbon materials have been applied as buffer layers in anode-free type ASSBs (AF-ASSBs). In these systems, carrier ions deposit on the negative current collector from the positive electrode active material during initial charging. This battery design improves energy density by reducing component materials and enhances cycle capability by

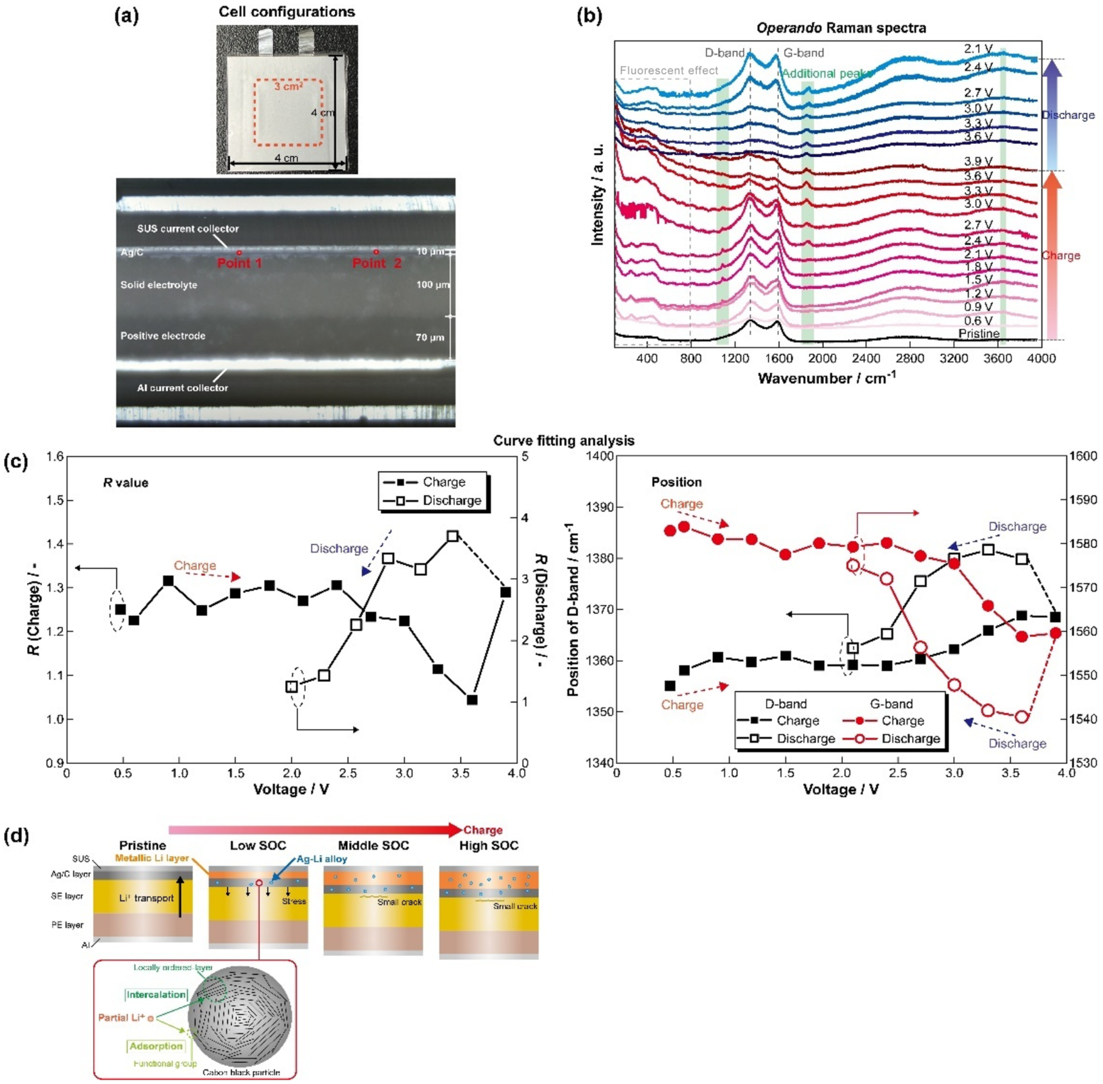

FIG. 7. Using *operando* Raman spectroscopy of the AF-ASSB with Ag/C layer to clarify the structural changes of amorphous CB under dynamic conditions. (a) Configuration of the laminate-type battery and the cross-sectional image indicating the measurement points. (b) *Operando* Raman spectra of the Ag/C layer taken every 0.3 V during the charge–discharge operation performed by sweeping the potential. (c) Calculated *R* values, defined as the ratio of the integrated intensities for the D-band and G-band, and peak positions of the D- and G-bands, obtained using the pseudo-Voigt function. (d) Illustration of the estimated reaction model for the cross-sectional AF-ASSB.

stabilizing ion deposition and dissolution on the current collector. In addition, a composite layer consisting of Ag nanoparticles and CB nanoparticles has been proposed by Samsung Co., Ltd.[69] In 2020, they reported an AF-ASSB incorporating an Ag/C layer between the solid electrolyte and negative current collector, achieving over 1000 cycles at high capacity and an energy density of 900 Wh l^{-1}. From *ex situ* XRD and TEM observations, they attributed this performance to reversible Ag–Li alloying and de-alloying reactions in the Ag/C layer during initial charging and discharging. However, the role of the Ag/C layer, including structural changes in CB during charge–discharge processes, remains unclear. Because CB is a disordered material, evaluating its structural changes using typical XRD techniques is challenging. *Operando* Raman spectroscopy is therefore a powerful tool for analyzing structural changes in disordered and amorphous materials during charge–discharge reactions.

We have evaluated the structural changes of CB in a sulfide-based AF-ASSB with an Ag/C layer using *operando*/*ex situ* Raman spectroscopy.[70] The AF-ASSB was used as a laminate-type cell composed of $LiNi_{0.9}Co_{0.05}Mn_{0.05}O_2$-based positive electrode, Li_6PS_5Cl-based solid electrolyte, and Ag/C layers, as shown in Fig. 7(a). This laminate AF-ASSB was cut and introduced into a measurement cell for *operando* Raman spectroscopy under an Ar atmosphere, using a glovebox. Pressure could be applied to this *operando* measurement cell to ensure stable charge–discharge reactions and prevent short circuits caused by Li dendrite growth. Short-circuit suppression is critical for *operando* measurements because cross-sectional samples have lower pressures than bulk samples. The CV profile obtained for the AF-ASSB with the Ag/C layer during *operando* Raman spectroscopy confirmed that redox reactions induced a current peak of ~3.6 V and a smaller current peak of ~0.6 V in the charging process, although localized short-circuiting occurred at 3.9 V owing to the insufficient pressure. Nonetheless, the short-circuited samples maintained a stable voltage of ~3.6 V under open-circuit conditions, and continuous discharging was observed. Figure 7(b) shows Raman spectra acquired every 0.3 V from the Ag/C layer during CV measurements (representative data from two measurement points). In the lower wavenumber region, a disordered baseline due to fluorescence effects was observed, suggesting a transition to a metallic state, corresponding to metallic Li deposition between the Ag/C layer and the SUS (stainless steel) current collector. Fluorescence effects inhibit the interpretation of the Raman spectra and thus the precise assignment of the peaks. However, in this AF-ASSB, the *in situ* formation of a metallic electrode layer facilitated monitoring of the degree of Li deposition during charging, owing to the differences in the Raman scattering properties between metallic and pristine states. In addition, the D- and G-bands, located at 1350 and 1580 cm^{-1}, respectively, showed significant changes in peak shape and position from their pristine state during charging. Quantitative analysis was conducted by curve fitting, revealing that the height ratio of the G-band to the D-band (R value) and changes in their positions indicated deviations in the graphene-stacked regularity and carbon structure during charge–discharge reactions, as shown in Fig. 7(c). This behavior likely reflects intercalation/deintercalation and/or adsorption/desorption of Li^+, consistent with similar phenomena reported in graphite-based active materials. Although disordered CB is traditionally considered to be electrochemically inactive, our study is the first to reveal structural changes in non-graphitized carbonaceous material during charging. The Ag/C layer serves as a buffer interlayer, facilitating current distribution through Ag–Li alloying and Li^+ intercalation reactions during charging, ultimately promoting stable Li deposition and dissolution [Fig. 7(d)]. *Operando* Raman spectroscopy enables detailed observation of the structural and morphological changes in disordered carbon materials at the micrometer scale, which cannot be detected using conventional XRD techniques designed for macroscopic structural evaluation. Applying this technique to disordered materials, particularly carbon, provides insights into electrochemical phenomena in various battery systems, such as weak interactions between graphitized compounds and Li^+ and associated structural changes. This capability supports the development of conductive additive materials by allowing researchers to optimize the material chemistry, structure, and surface morphology.

D. Multi-scale analysis of oxide-based all-solid-state batteries

Charge–discharge reactions in battery systems are highly complex, proceeding through hierarchical and interconnected steps. In electrode layers, these reactions primarily involve redox processes among transition metal elements, ionic diffusion, and electron acceptance in active materials. Electrolyte layers contribute to ionic transport between electrodes, within the composite electrodes, and at their interfaces. Furthermore, structural and morphological changes occur at the same time scale as these mass transport processes. Consequently, achieving a comprehensive understanding of charge–discharge reactions remains a challenge. *Operando* measurement techniques are critical because they enable direct observation of electrochemical reactions, including structural, morphological, elemental, and electron state changes during charge–discharge cycles. However, single-scale *operando* measurement techniques are often insufficient for capturing all processes occurring in the charge–discharge operation, which often includes multi-step electrochemical reactions. To address this limitation, we proposed a multi-scale analysis approach that combines *operando* elemental and spectroscopic measurement techniques to investigate reactions occurring at a range of scales, from the atomic to the micrometer level, employing SEM-EDS, Raman spectroscopy, and time-of-flight secondary ion mass spectrometry (TOF-SIMS). This section introduces the challenges of multi-scale analysis, particularly for using *operando* Raman spectroscopy to study charge–discharge reactions in ASSBs.[71]

In this work, we selected an oxide-type ASSB using Na as the carrier ion, comprising $Na_3V_2(PO_4)_3$ (NVP) as both the positive and negative electrode active materials and NZSP as the solid electrolyte, considering the resource abundance and low Young's modulus compared with those with Li-based systems. The ASSB was prepared by multi-step spark plasma sintering, using B_2O_3 as an adhesive material to achieve a low melting point and improve pellet density. For multi-scale analysis, we used an electrochemical measurement holder/cell capable of applying voltage, as shown in Fig. 8(a). The holder/cell allowed the sample to be inserted and removed, facilitating transfer between the SEM-EDS and Raman spectroscopy equipment. The ASSB sample was polished by Ar^+ milling to reveal the cross section and then placed in the SEM-EDS holder under an Ar atmosphere [see Fig. 8(a)]. *Operando* SEM-EDS was conducted from the positive to the negative electrode (distance: ~200 μm) during the first charge–discharge cycle. Figure 8(b) shows the elemental

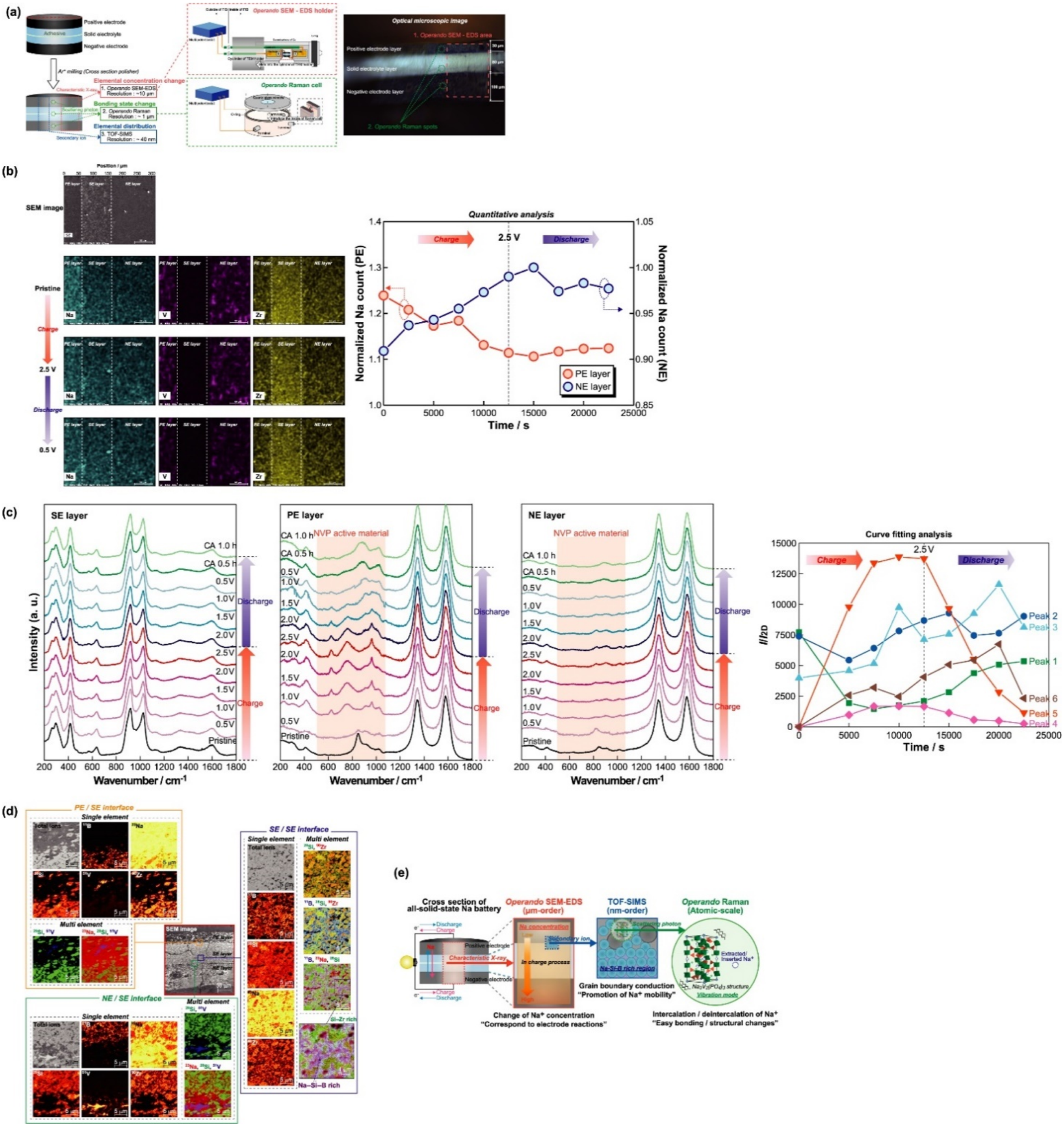

FIG. 8. Using a multi-scale analysis approach to comprehensively characterize an oxide-type Na-ASSB with NVP electrode active materials. (a) Illustration of the multi-scale analysis technique used for characterizing the oxide-type ASSB and a cross-sectional image indicating the areas used for *operando* SEM-EDS, *operando* Raman, and TOF-SIMS. (b) SEM image of the EDS mapping area in the pristine state and EDS mapping of the Na, V, and Si acquired during the charge–discharge operation (left), as well as changes in the amount of Na normalized by the V and Si counts (right), all observed by *operando* SEM-EDS measurement during the first charge–discharge cycle. Note that the Na, V, and Si elements correspond to NVP/NZSP, NVP, and NZSP. (c) Raman spectra of the solid electrolyte (SE), positive electrode (PE), and negative electrode (NE) layers in the 200–1800 cm^{-1} range, and time dependencies of the integrated intensity changes normalized by the 2D-band of carbon (I/I_{2D}) calculated from curve fitting, all observed by *operando* Raman measurement during the second charge–discharge cycle. (d) SEM image of the observation area (center), and TOF-SIM images of the ^{11}B, ^{23}Na, ^{28}Si, ^{51}V, and ^{90}Zr at the PE/SE (left), SE/SE (right), and NE/SE (lower) interfaces, acquired in the positive ion mode after running the third charge–discharge cycle. Reproduced with permission from K. Hiraoka *et al.*, Energy Environ. Mater., 1–10 (2024). Copyright 2024 John Wiley & Sons.

mappings of Na and their normalized counts as a function of voltage. Na distributions changed slightly during the charge–discharge operation, with clear decreases and increases observed in the positive and negative electrode layers, corresponding to Na deintercalation and intercalation in the NVP active material. Subsequently, *operando* Raman spectroscopy was performed at intermediate points within the positive electrode, negative electrode, and solid electrolyte layers using a laser spot size of ~1 μm, during the second charge–discharge cycle. Raman spectra were acquired every 0.3 V at each point, with a calculated time resolution of 360 s. Figure 8(c) shows the Raman spectra in each layer, the results of curve fitting, and the integrated intensities (I/I_{2D}) normalized to the 2D-band of the carbon (conductive additive) in the positive electrode layer in the 200–1800 cm^{-1} range. During charging, the spectral intensity increased in the positive electrode layer, and new components appeared in the 200–1800 cm^{-1} range. These changes reversed during discharging, and peak separation revealed that Raman-active components increased from 3 to 6 in this wavenumber range. In addition, I/I_{2D} for peak 5 showed significant increases and decreases during charging and discharging, respectively. These findings suggest that structural changes in NVP were associated with activated vibrational modes of the PO_4 tetrahedron (e.g., distortion and twisting) during Na$^+$ intercalation/deintercalation. Finally, TOF-SIMS analysis was performed on the negative electrode–solid electrolyte, solid electrolyte–solid electrolyte, and negative electrode–solid electrolyte interfaces after running the third charge–discharge cycle [Fig. 8(d)]. TOF-SIMS provided high-contrast elemental mapping with ~40 nm spatial resolution. Notably, specific features were observed near the grain boundary region in the solid electrolyte layer. The grain boundary region contained ^{11}B (adhesive, namely B_2O_3), ^{23}Na (NVP and NZSP), and ^{27}Si (NZSP), indicating that Na$^+$ migrates along this pathway during charge–discharge operations. By combining these results, we revealed the Na concentration changes in the electrode layers, crystal structure changes in the active material, and Na$^+$ migration pathways near the grain boundaries in the ASSB. *Operando* SEM-EDS/Raman spectroscopy and TOF-SIMS contributed complementary insights at different scales: Raman spectroscopy was leveraged to monitor atomic-scale crystal structure changes, whereas SEM-EDS provided micrometer-scale elemental distribution data, and TOF-SIMS captured nanometer-scale conduction pathways. This multi-scale analytical approach demonstrates the advanced capability of *operando* Raman spectroscopy, in conjunction with other techniques, to comprehensively evaluate electrochemical phenomena and structural changes in ASSBs.

IV. CONCLUSIONS AND OUTLOOK

This review paper covers the application of Raman spectroscopy, ranging from static to dynamic (*operando*) measurements, for various battery systems. In static analyses, Raman spectroscopy provides insights into the atomic-scale structures of the component materials, such as liquid electrolytes and electrode materials. For liquid electrolytes with highly concentrated salt, Raman spectroscopy reveals solvation structures formed by coordination between solvents, anions, and cations that facilitate Li$^+$ conduction. This helps elucidate the physicochemical and electrochemical properties of these systems. In addition, Raman spectroscopy effectively characterizes multiple-phase electrode materials, such as nanoparticle Si and amorphous carbon, which are difficult to analyze using conventional XRD techniques, even under static conditions. For unstable materials, changes in crystal structure and the formation of by-products can be detected by controlling the atmosphere and cell configuration, as demonstrated for NCO electrode active materials. Notably, imaging combined with MCR analysis enables visualization of the material distributions and components within composite electrode sheets.

Advanced *operando* Raman spectroscopy techniques have been introduced, providing insights into ionic transport, cycling degradation, and electrode reaction mechanisms in different battery systems. These include Li/Na symmetrical cells using SPEs, oxide-type ASSBs with asymmetric electrodes, sulfide-type ASSBs with the Ag/C interlayers, and oxide-type ASSBs with symmetrical electrodes under electrochemical reactions. For symmetrical cells using SPEs, differences in Li$^+$ and Na$^+$ concentration changes under DC polarization strongly correlate with the solvation structures of the host polymer in the initial state. In oxide-type ASSBs with NNPP and NTP as the positive and negative electrode layers, respectively, *operando* Raman spectroscopy revealed that cycling-induced crystal structure degradation of active materials significantly decreased the capacity and reaction current while forming by-products during cell fabrication. In sulfide-type ASSBs, the role of the Ag/C layer during charging/discharging was previously unclear, but *operando* Raman spectroscopy showed that disordered CB in the Ag/C layer partially reacted with Li$^+$ via intercalation, contributing to stable Li deposition during charging and suppressing dendrite formation. Furthermore, multi-scale analysis was demonstrated for oxide-type ASSBs using NVP as both the positive and negative electrode active materials. By using *operando* SEM-EDS, Raman spectroscopy, and TOF-SIMS on the same cell, we comprehensively analyzed the charge–discharge reactions. *Operando* SEM-EDS and Raman spectroscopy captured Na concentration changes at the micrometer scale and crystal structure/bonding state changes at the atomic scale, respectively, during individual charge–discharge cycles. TOF-SIMS was performed after running an additional cycle, providing precise mappings of the elemental distributions at the nanometer scale, particularly in the grain boundary regions of the solid electrolyte, revealing the Na$^+$ conduction pathways during charge–discharge processes. Based on these studies under both static and dynamic conditions, Raman spectroscopy has proven to be a powerful tool for characterizing a wide range of materials and for directly observing electrochemical and structural changes in real time. This capability not only yields detailed structural information derived from molecular vibrations and electric polarization but also elucidates the hierarchical processes occurring during charge–discharge cycling within battery systems.

To further advance the application of Raman spectroscopy in the battery field, the following improvements are recommended:

(1) Enhancing spatial and temporal resolutions

Battery materials, particularly electrode active materials, often contain particle sizes on the order of ~10 μm, whereas the typical spatial resolution of Raman spectroscopy is ~1–5 μm. This makes it difficult to differentiate structural or chemical distributions across individual particles or distinguish phenomena occurring inside and outside of the particles. In addition, depending on the Raman activity of the material, acquiring Raman spectra with sufficient intensity often requires seconds to minutes. In *operando* Raman spectroscopy, low temporal resolution hinders the ability to capture hierarchically complex electrochemical reactions and structural/vibrational state changes on relevant time scales. Future developments in high-sensitivity detectors and tip-enhanced Raman spectroscopy are necessary to improve the signal-to-noise ratio and enhance the spatial resolution.

(2) Applying for Raman-inactive and weakly active materials

Battery materials sometimes exhibit Raman-inactivity or weak activity due to their molecular polarizability. To address this challenge, it is essential to minimize background noise and fluorescence effects in order to improve the signal-to-noise ratio in both static and dynamic (*operando*) measurements. One effective approach is to select an appropriate excitation wavelength, which helps reduce fluorescence effects associated with the material's polarization properties. In addition to wavelength selection, SERS can further enhance Raman signals at a microscopic scale. By combining SERS with precise peak assignment through simulations (e.g., density functional theory), significant improvements in *operando* Raman spectroscopy are expected, enabling rapid capture of electrochemical and structural reactions when integrated with the methods discussed in Sec. III D.

(3) Integration with other analytical techniques

Charge–discharge reactions are extremely complex, including various reactions at the atomic and micrometer scales. Raman spectroscopy alone, even with *operando* techniques, is insufficient for fully understanding these processes. Elemental and electronic analytical techniques are key tools for evaluating ionic concentration, valence changes in electrodes, decomposition layer formation at electrode/electrolyte interfaces, and more. While a multi-scale analysis framework has been established, further diversification of the analytical techniques, such as SEM/TEM and synchrotron spectroscopy, may be necessary. These techniques can provide extended structural, morphological, and elemental information for a more comprehensive characterization of the charge–discharge reactions.

ACKNOWLEDGMENTS

This article is based on results obtained from the Feasibility Study Program and Intensive Support Program for Young Promising Researchers commissioned by the New Energy and Industrial Technology Development Organization (NEDO). We thank Professor Yasuhiro Umebayashi (Niigata Univ.), Mr. Takao Kunimi (Sumitomo Bakelite), Dr. Takeshi Kobayashi (CRIEPI), Professor Tetsuo Sakamoto (Kogakuin Univ.), Dr. Naoki Suzuki, and Dr. Tetsuya Asano (Samsung Japan).

AUTHOR DECLARATIONS

Conflict of Interest

The authors have no conflicts to disclose.

Author Contributions

Koji Hiraoka: Conceptualization (equal); Data curation (lead); Funding acquisition (equal); Investigation (lead); Supervision (equal); Validation (equal); Writing – original draft (lead); Writing – review & editing (equal). **Yoshiki Yokoyama**: Data curation (lead); Investigation (supporting); Writing – original draft (equal); Writing – review & editing (equal). **Sarina Mine**: Data curation (equal); Investigation (equal); Writing – original draft (equal). **Kazuo Yamamoto**: Data curation (equal); Investigation (equal); Validation (equal); Writing – review & editing (equal). **Shiro Seki**: Conceptualization (equal); Funding acquisition (equal); Supervision (equal); Validation (equal); Writing – original draft (equal); Writing – review & editing (equal).

DATA AVAILABILITY

Data sharing is not applicable to this article as no new data were created or analyzed in this study.

REFERENCES

[1] B. Obama, "The irreversible momentum of clean energy," Science **355**, 126–129 (2017).

[2] O. Smith, O. Cattell, E. Farcot, R. D. O'Dea, and K. I. Hopcraft, "The effect of renewable energy incorporation on power grid stability and resilience," Sci. Adv. **8**, 6734–6743 (2022).

[3] A. A. Franco, A. Rucci, D. Brandell, C. Frayret, M. Gaberscek, P. Jankowski, and P. Johansson, "Boosting rechargeable batteries R&D by multiscale modeling: Myth or reality?," Chem. Rev. **119**, 4569–4627 (2019).

[4] Z. Zhu, T. Jiang, M. Ali, Y. Meng, Y. Jin, Y. Cui, and W. Chen, "Rechargeable batteries for grid scale energy storage," Chem. Rev. **122**, 16610–16751 (2022).

[5] B. Dunn, H. Kamath, and J.-M. Tarascon, "Electrical energy storage for the grid: A battery of choices," Science **334**, 928–935 (2011).

[6] M. Winter, B. Barnett, and K. Xu, "Before Li ion batteries," Chem. Rev. **118**, 11433–11456 (2018).

[7] K. Liu, Y. Liu, D. Lin, A. Pei, and Y. Cui, "Materials for lithium-ion battery safety," Sci. Adv. **4**, eaas9820 (2018).

[8] R. Marom, S. F. Amalraj, N. Leifer, D. Jacob, and D. Aurbach, "A review of advanced and practical lithium battery materials," J. Mater. Chem. **21**, 9938 (2011).

[9] A. Y. S. Eng, C. B. Soni, Y. Lum, E. Khoo, Z. Yao, S. K. Vineeth, V. Kumar, J. Lu, C. S. Johnson, C. Wolverton, and Z. W. Seh, "Theory-guided experimental design in battery materials research," Sci. Adv. **8**, eabm2422 (2022).

[10] E. P. Alsaç, D. L. Nelson, S. G. Yoon, K. A. Cavallaro, C. Wang, S. E. Sandoval, U. D. Eze, W. J. Jeong, and M. T. McDowell, "Characterizing electrode materials and interfaces in solid-state batteries," Chem. Rev. **4**, 2009–2119 (2025).

[11] M. S. Whittingham, "Ultimate limits to intercalation reactions for lithium batteries," Chem. Rev. **114**, 11414–11443 (2014).

[12] J. Li, J. Fleetwood, W. B. Hawley, and W. Kays, "From materials to cell: State-of-the-art and prospective technologies for lithium-ion battery electrode processing," Chem. Rev. **122**, 903–956 (2022).

[13] D. Zhou, D. Shanmukaraj, A. Tkacheva, M. Armand, and G. Wang, "Polymer electrolytes for lithium-based batteries: Advances and prospects," Chem **5**, 2326–2352 (2019).

[14] Y.-K. Liu, C.-Z. Zhao, J. Du, X. Zhang, A.-B. Chen, and Q. Zhang, "Research progresses of liquid electrolytes in lithium-ion batteries," Small **19**, 2205315 (2023).

[15] A. Manthiram, X. Yu, and S. Wang, "Lithium battery chemistries enabled by solid-state electrolytes," Nat. Rev. Mater. **2**, 16103 (2017).

[16] M. S. Whittingham, "Special editorial perspective: Beyond Li-ion battery chemistry," Chem. Rev. **120**, 6328–6330 (2020).

[17] M. Park, X. Zhang, M. Chung, G. B. Less, and A. M. Sastry, "A review of conduction phenomena in Li-ion batteries," J. Power Sources **195**, 7904–7929 (2010).

[18] Y.-M. Chiang, "Building a better battery," Science **330**, 1485–1486 (2010).

[19] T. Famprikis, P. Canepa, J. A. Dawson, M. S. Islam, and C. Masquelier, "Fundamentals of inorganic solid-state electrolytes for batteries," Nat. Mater. **18**, 1278–1291 (2019).

[20] J. Cabana, L. Monconduit, D. Larcher, and M. R. Palacín, "Beyond intercalation-based Li-ion batteries: The state of the art and challenges of electrode materials reacting through conversion reactions," Adv. Mater. **22**, E170–E192 (2010).

[21] T. Waldmann, A. Iturrondobeitia, M. Kasper, N. Ghanbari, F. Aguesse, E. Bekaert, L. Daniel, S. Genies, I. J. Gordon, M. W. Löble, E. De Vito, and M. Wohlfahrt-Mehrens, "Review—Post-mortem analysis of aged lithium-ion batteries: Disassembly methodology and physico-chemical analysis techniques," J. Electrochem. Soc. **163**, A2149–A2164 (2016).

[22] R. F. Ziesche, T. M. M. Heenan, P. Kumari, J. Williams, W. Li, M. E. Curd, T. L. Burnett, I. Robinson, D. J. L. Brett, M. J. Ehrhardt, P. D. Quinn, L. B. Mehdi, P. J. Withers, M. M. Britton, N. D. Browning, and P. R. Shearing, "Multi-dimensional characterization of battery materials," Adv. Energy Mater. **13**, 2300103 (2023).

[23] S. Bertilsson, F. Larsson, M. Furlani, I. Albinsson, and B.-E. Mellander, "Lithium-ion battery electrolyte emissions analyzed by coupled thermogravimetric/Fourier-transform infrared spectroscopy," J. Power Sources **365**, 446–455 (2017).

[24] M. Mroczkowska, J. L. Nowinski, G. Z. Zukowska, A. Mroczkowska, J. E. Garbarczyk, M. Wasiucionek, and S. Gierlotka, "Micro Raman, FT-IR/PAS, XRD and SEM studies on glassy and partly crystalline silver phosphate ionic conductors," J. Power Sources **173**, 729–733 (2007).

[25] R. Baddour-Hadjean and J.-P. Pereira-Ramos, "Raman microspectrometry applied to the study of electrode materials for lithium batteries," Chem. Rev. **110**, 1278–1319 (2010).

[26] A. C. Ferrari, "Raman spectroscopy of graphene and graphite: Disorder, electron–phonon coupling, doping and nonadiabatic effects," Solid State Commun. **143**, 47–57 (2007).

[27] "Improving the fundamental understanding of batteries via *operando* measurements," Nat. Commun. **13**, 4723 (2022).

[28] Y. Yamada, J. Wang, S. Ko, E. Watanabe, and A. Yamada, "Advances and issues in developing salt-concentrated battery electrolytes," Nat. Energy **4**, 269–280 (2019).

[29] S. Chen, J. Zheng, D. Mei, K. S. Han, M. H. Engelhard, W. Zhao, W. Xu, J. Liu, and J.-G. Zhang, "High-voltage lithium-metal batteries enabled by localized high-concentration electrolytes," Adv. Mater. **30**, 1706102 (2018).

[30] Y. Yamada, K. Furukawa, K. Sodeyama, K. Kikuchi, M. Yaegashi, Y. Tateyama, and A. Yamada, "Unusual stability of acetonitrile-based superconcentrated electrolytes for fast-charging lithium-ion batteries," J. Am. Chem. Soc. **136**, 5039–5046 (2014).

[31] S. Saito, H. Watanabe, K. Ueno, T. Mandai, S. Seki, S. Tsuzuki, Y. Kameda, K. Dokko, M. Watanabe, and Y. Umebayashi, "Li$^+$ local structure in hydrofluoroether diluted Li-glyme solvate ionic liquid," J. Phys. Chem. B **120**, 3378–3387 (2016).

[32] R. Furui, K. Hayamizu, K. Takahashi, S. Tsuzuki, H. Miyauchi, K. Inaba, Y. Kawana, Y. Umebayashi, and S. Seki, "Elucidation of liquid structures and transport properties of highly concentrated LiN(SO$_2$F)$_2$/ethylene carbonate electrolytes," J. Phys. Chem. C **127**, 10748–10756 (2023).

[33] A. Yoshino, "The birth of the lithium-ion battery," Angew. Chem., Int. Ed. **51**, 5798–5800 (2012).

[34] M. Ge, C. Cao, G. M. Biesold, C. D. Sewell, S.-M. Hao, J. Huang, W. Zhang, Y. Lai, and Z. Lin, "Recent advances in silicon-based electrodes: From fundamental research toward practical applications," Adv. Mater. **33**, 2004577 (2021).

[35] U. Tsunoda, K. Hiraoka, Y. Kobayashi, T. Kunimi, and S. Seki, "Degradation suppression effect of amorphous-hard-carbon-bundled Si-based negative electrode," Mater. Adv. **4**, 4436–4443 (2023).

[36] T. Ichikawa, K. Hiraoka, and S. Seki, "Interfacial modification of NaCoO$_2$ positive electrodes with inorganic oxides by simple mixing and the effects on all-solid-state Na batteries," RSC Adv. **14**, 19726–19734 (2024).

[37] V. G. Hadjiev, M. N. Iliev, and I. V. Vergilov, "The Raman spectra of Co$_3$O$_4$," J. Phys. C: Solid State Phys. **21**, L199–L201 (1988).

[38] M. Inaba, Y. Iriyama, Z. Ogumi, Y. Todzuka, and A. Tasaka, "Raman study of layered rock-salt LiCoO$_2$ and its electrochemical lithium deintercalation," J. Raman Spectrosc. **28**, 613–617 (1997).

[39] J. Wu, G. K. P. Dathar, C. Sun, M. G. Theivanayagam, D. Applestone, A. G. Dylla, A. Manthiram, G. Henkelman, J. B. Goodenough, and K. J. Stevenson, "*In situ* Raman spectroscopy of LiFePO$_4$: Size and morphology dependence during charge and self-discharge," Nanotechnology **24**, 424009 (2013).

[40] F. Lin, Y. Liu, X. Yu, L. Cheng, A. Singer, O. G. Shpyrko, H. L. Xin, N. Tamura, C. Tian, T.-C. Weng, X.-Q. Yang, Y. S. Meng, D. Nordlund, W. Yang, and M. M. Doeff, "Synchrotron X-ray analytical techniques for studying materials electrochemistry in rechargeable batteries," Chem. Rev. **117**, 13123–13186 (2017).

[41] D. Liu, Z. Shadike, R. Lin, K. Qian, H. Li, K. Li, S. Wang, Q. Yu, M. Liu, S. Ganapathy, X. Qin, Q.-H. Yang, M. Wagemaker, F. Kang, X.-Q. Yang, and B. Li, "Review of recent development of in situ/operando characterization techniques for lithium battery research," Adv. Mater. **31**, 1806620 (2019).

[42] I. López, J. Morey, J. B. Ledeuil, L. Madec, and H. Martinez, "A critical discussion on the analysis of buried interfaces in Li solid-state batteries. *Ex situ* and *in situ/operando* studies," J. Mater. Chem. A **9**, 25341–25368 (2021).

[43] J. Maibach, J. Rizell, A. Matic, and N. Mozhzhukhina, "Toward *operando* characterization of interphases in batteries," ACS Mater. Lett. **5**, 2431–2444 (2023).

[44] O. M. Magnussen, J. Drnec, C. Qiu, I. Martens, J. J. Huang, R. Chattot, and A. Singer, "*In situ* and *operando* X-ray scattering methods in electrochemistry and electrocatalysis," Chem. Rev. **124**, 629–721 (2024).

[45] X. Wei, X. Wang, Q. An, C. Han, and L. Mai, "Operando X-ray diffraction characterization for understanding the intrinsic electrochemical mechanism in rechargeable battery materials," Small Methods **1**, 1700083 (2017).

[46] B.-K. Cho, S.-Y. Jung, S.-J. Park, J.-H. Hyun, and S.-H. Yu, "*In situ/operando* imaging techniques for next-generation battery analysis," ACS Energy Lett. **9**, 4068–4092 (2024).

[47] P. Pietsch and V. Wood, "X-ray tomography for lithium ion battery research: A practical guide," Annu. Rev. Mater. Res. **47**, 451–479 (2017).

[48] D. Cheng, J. Hong, D. Lee, S.-Y. Lee, and H. Zheng, "*In situ* TEM characterization of battery materials," Chem. Rev. **125**, 1840–1896 (2025).

[49] W. Cheng, M. Zhao, Y. Lai, X. Wang, H. Liu, P. Xiao, G. Mo, B. Liu, and Y. Liu, "Recent advances in battery characterization using in situ XAFS, SAXS, XRD, and their combining techniques: From single scale to multiscale structure detection," Exploration **4**, 20230056 (2024).

[50] Q. Chang, Y. X. Angel Ng, D. Yang, J. Chen, T. Liang, S. Chen, X. Zhang, Z. Ou, J. Kim, E. H. Ang, H. Xiang, and X. Song, "Quantifying the morphology evolution of lithium battery materials using operando electron microscopy," ACS Mater. Lett. **5**, 1506–1526 (2023).

[51] D. Alves Dalla Corte, G. Caillon, C. Jordy, J.-N. Chazalviel, M. Rosso, and F. Ozanam, "Spectroscopic insight into Li-ion batteries during operation: An alternative infrared approach," Adv. Energy Mater. **6**, 1501768 (2016).

[52] E. Flores, P. Novák, and E. J. Berg, "*In situ* and *operando* Raman spectroscopy of layered transition metal oxides for Li-ion battery cathodes," Front. Energy Res. **6**, 82 (2018).

[53] R. Zhang, Y. Wu, Z. Chen, Y. Wang, J. Zhu, and X. Zhuang, "The value of *in situ*/operando Raman spectroscopy in all-solid-state Li batteries," J. Mater. Chem. A **11**, 19195–19209 (2023).

[54] M. Moskovits, "Surface-enhanced spectroscopy," Rev. Mod. Phys. **57**, 783–826 (1985).

[55] S. Hy, Felix, Y.-H. Chen, J.-Y. Liu, J. Rick, and B.-J. Hwang, "*In situ* surface enhanced Raman spectroscopic studies of solid electrolyte interphase formation in lithium ion battery electrodes," J. Power Sources **256**, 324–328 (2014).

[56] J. Fawdon, J. Ihli, F. L. Mantia, and M. Pasta, "Characterising lithium-ion electrolytes via operando Raman microspectroscopy," Nat. Commun. **12**, 4053 (2021).

[57] Y. Ishino, T. Yamamoto, K. Manabe, and T. Nohira, "In-situ Raman spectroscopic analysis of factors improving discharge rate capability of Na-ion batteries with FSA-based ionic liquids," Electrochemistry **92**, 1900197 (2024).

[58] I. Rey, J.-L. Bruneel, J. Grondin, L. Servant, and J.-C. Lassègues, "Raman spectroelectrochemistry of a lithium/polymer electrolyte symmetric cell," J. Electrochem. Soc. **145**, 3034–3042 (1998).

[59] P. Georén, J. Adebahr, P. Jacobsson, and G. Lindbergh, "Concentration polarization of a polymer electrolyte," J. Electrochem. Soc. **149**, A1015 (2002).

[60] K. Hiraoka and S. Seki, "*Operando* Raman spectroscopy for evaluating concentration changes in Li- and Na-based solid polymer electrolytes," J. Phys. Chem. C **127**, 11864–11874 (2023).

[61] T. Yoshida, M. Takahashi, S. Morikawa, C. Ihara, H. Katsukawa, T. Shiratsuchi, and J. Yamaki, "Degradation mechanism and life prediction of lithium-ion batteries," J. Electrochem. Soc. **153**, A576 (2006).

[62] D. Li, D. L. Danilov, L. Gao, Y. Yang, and P. H. L. Notten, "Degradation mechanisms of C_6/$LiFePO_4$ batteries: Experimental analyses of cycling-induced aging," Electrochim. Acta **210**, 445–455 (2016).

[63] T. Ono, K. Hiraoka, T. Kobayashi, K. Yamamoto, and S. Seki, "Degradation analysis of oxide-based all-solid-state Na batteries by *operando* Raman spectroscopy," ACS Appl. Energy Mater. **6**, 6194–6200 (2023).

[64] M. Nose, H. Nakayama, K. Nobuhara, H. Yamaguchi, S. Nakanishi, and H. Iba, "$Na_4Co_3(PO_4)_2P_2O_7$: A novel storage material for sodium-ion batteries," J. Power Sources **234**, 175–179 (2013).

[65] M. Wu, W. Ni, J. Hu, and J. Ma, "NASICON-structured $NaTi_2(PO_4)_3$ for sustainable energy storage," Nano-Micro Lett. **11**, 44 (2019).

[66] A. C. Ferrari and J. Robertson, "Interpretation of Raman spectra of disordered and amorphous carbon," Phys. Rev. B **61**, 14095–14107 (2000).

[67] Y. Domi, T. Doi, H. Nakagawa, T. Yamanaka, T. Abe, and Z. Ogumi, "In situ Raman study on reversible structural changes of graphite negative-electrodes at high potentials in $LiPF_6$-based electrolyte solution," J. Electrochem. Soc. **163**, A2435–A2440 (2016).

[68] D. Aurbach and Y. Ein-Eli, "The study of Li-graphite intercalation processes in several electrolyte systems using *in situ* X-ray diffraction," J. Electrochem. Soc. **142**, 1746–1752 (1995).

[69] Y. G. Lee, S. Fujiki, C. Jung, N. Suzuki, N. Yashiro, R. Omoda, D. S. Ko, T. Shiratsuchi, T. Sugimoto, S. Ryu, J. H. Ku, T. Watanabe, Y. Park, Y. Aihara, D. Im, and I. T. Han, "High-energy long-cycling all-solid-state lithium metal batteries enabled by silver–carbon composite anodes," Nat. Energy **5**, 299–308 (2020).

[70] K. Hiraoka, J. Sakabe, N. Suzuki, and S. Seki, "*Operando* and *ex-situ* Raman spectroscopies for Evaluating Carbon Structural Changes in Anode-Free-Type Sulfide-Based All-Solid-State Li Battery" (submitted) (2025).

[71] K. Hiraoka, K. Yamamoto, T. Kobayashi, T. Sakamoto, and S. Seki, "Multi-scale analysis combined *operando* elemental/spectroscopic measurement techniques in oxide-type all-solid-state Na batteries," Energy Environ. Mater. **8**, e12821 (2024).